Two-Dimensional Tracking of ncd Motility by Back Focal Plane Interferometry

Miriam W. Allersma,* Frederick Gittes,* Michael J. deCastro,# Russell J. Stewart,# and Christoph F. Schmidt*
*Department of Physics and Biophysics Research Division, University of Michigan, Ann Arbor, Michigan 48109, and #Department of Bioengineering, University of Utah, Salt Lake City, Utah 84105 USA

ABSTRACT A technique for detecting the displacement of micron-sized optically trapped probes using far-field interference is introduced, theoretically explained, and used to study the motility of the ncd motor protein. Bead motions in the focal plane relative to the optical trap were detected by measuring laser intensity shifts in the back-focal plane of the microscope condenser by projection on a quadrant diode. This detection method is two-dimensional, largely independent of the position of the trap in the field of view and has ~10-μs time resolution. The high resolution makes it possible to apply spectral analysis to measure dynamic parameters such as local viscosity and attachment compliance. A simple quantitative theory for back-focal-plane detection was derived that shows that the laser intensity shifts are caused primarily by a far-field interference effect. The theory predicts the detector response to bead displacement, without adjustable parameters, with good accuracy. To demonstrate the potential of the method, the ATP-dependent motility of ncd, a kinesin-related motor protein, was observed with an in vitro bead assay. A fusion protein consisting of truncated ncd (amino acids 195–685) fused with glutathione-S-transferase was adsorbed to silica beads, and the axial and lateral motions of the beads along the microtubule surface were observed with high spatial and temporal resolution. The average axial velocity of the ncd-coated beads was 230 ± 30 nm/s (average ± SD). Spectral analysis of bead motion showed the increase in viscous drag near the surface; we also found that any elastic constraints of the moving motors are much smaller than the constraints due to binding in the presence of the nonhydrolyzable nucleotide adenylylimidodiphosphate.

INTRODUCTION

The kinesins are motor proteins responsible for intracellular transport along microtubules of the cytoskeleton. Many active motion processes in eukaryotic cells have been found to be associated with a unique kinesin, or kinesins (for a recent review see Moore and Endow, 1996), prompting a great deal of research focusing on the functional principles of these proteins. Most members of the kinesin family move toward the microtubule plus-end, but some have been found to move toward the minus-end, for example, the ncd and kar3 proteins (McDonald and Goldstein, 1990; Walker et al., 1990; Endow et al., 1994; Kuriyama et al., 1995). Although they move in opposite directions, the motor domains of ncd and kinesin are 43% identical in amino acid sequence (Endow et al., 1990; McDonald and Goldstein, 1990) and have strikingly similar three-dimensional structures (Kull et al., 1996; Sablin et al., 1996). The directionality of kinesin and ncd is likely to be determined within the head domains including the neck region (Stewart et al., 1993; Case et al., 1997; Henningsen and Schliwa, 1997), but the specific microscopic determinants of directionality are not yet known.

Kinesin, originally isolated from squid giant axons (Brady, 1985; Vale et al., 1985), is highly processive; a single dimeric kinesin motor can transport microtubules over many microns, representing hundreds of enzymatic cycles (Howard et al., 1989; Block et al., 1990; Svoboda et al., 1993; Vale et al., 1996). A feature of kinesin's processive mechanism is its path on the surface of microtubules. Video tracking of kinesin-coated beads (Gelles et al., 1988; Wang et al., 1995) and observation of helical tracking of kinesin along supertwisted microtubules (Ray et al., 1993) demonstrated that kinesin dimers follow a single protofilament. Single-headed kinesin, in contrast, supports motility only in large numbers. Beads driven by multiple single-headed kinesins did not appear to follow a straight path along the microtubule surface in video tracking experiments (Berliner et al., 1995), which suggested that kinesin's processivity is due to interactions between the two heads of a dimer. Similar experiments to investigate the path of dimeric ncd have not been reported.

A variety of optical techniques capable of detecting nanometer displacements with high temporal resolution have been developed and applied to studying motor proteins and other biological molecules. Fine glass needles, imaged onto split photodiodes, have been used to observe motions and mechanical responses of myosin (VanBuren et al., 1994; Ishijima et al., 1996) and kinesin (Meyhöfer and Howard, 1995) with nanometer displacement resolution. Similarly, imaging micron-sized beads onto split photodiodes has been used to detect unitary translocation events of myosin (Finer et al., 1994; Simmons et al., 1996) and kinesin molecules (Coppin et al., 1996; Higuchi et al., 1997).

In addition to direct imaging techniques, several phase-sensitive, interferometric detection methods have been de-

Received for publication 14 July 1997 and in final form 7 November 1997.
Address reprint requests to Dr. Christoph Schmidt, Biophysics Research Division, University of Michigan, 930 North University, Chemistry Bldg., Ann Arbor, MI 48109-1055. Tel.: 313-763-9139; Fax: 313-764-3323; E-mail: cfs@umich.edu.

0006-3495/98/02/1074/12 $2.00

veloped. A spot-focused form of differential interference contrast (DIC) microscopy (Nomarski, 1955; Smith, 1955; Allen et al., 1969) was introduced (Denk and Webb, 1990) that detects the relative phase lag caused by a refractive object between two overlapping, orthogonally polarized laser foci. The method provides uniaxial subnanometer displacement resolution along the direction of the offset between the foci, while measuring the displacement relative to the foci. The detecting laser focus can simultaneously serve as an optical trap (Ashkin et al., 1986; Svoboda and Block, 1994a). The combination of optical trapping and interferometric detection has been used to study kinesin (Svoboda et al., 1993; Svoboda and Block, 1994b; Yin et al., 1995), the mechanical properties of DNA (Smith et al., 1996; Wang et al., 1997), and properties of F-actin gels (Gittes et al., 1997; Schnurr et al., 1997).

Other nonimaging displacement detection techniques generally share the use of split photodiodes to detect diffraction or interference patterns in the trapping laser light. Spatial detection of interference in scanned beam microscopes was first applied to generate phase contrast in scanning transmission electron microscopy (STEM) (Dekkers and de Lang, 1974; Dekkers and de Lang, 1977) and later in laser scanning microscopy (Wilson, 1988). Ghislain and colleagues (Ghislain and Webb, 1993; Ghislain et al., 1994) reported a technique to measure axial and lateral displacements in an optical trap by placing a photodiode between the back-focal plane of the microscope condenser and the intermediate image plane. Smith et al. (1996) reported a related displacement detection scheme in a laser trap formed by two counter-propagating laser beams of low numerical aperture, and Visscher et al. (1996) reported a further variation of the scheme using separate lasers for trapping and detection. When one laser is used for both trapping and detection, displacement is always measured with respect to the center of the trap. With independent lasers, displacement can be measured independent of trap position.

The major advantage of the detection methods based on photodiodes and laser illumination is that nanometer displacements can be measured with bandwidths up to 100 kHz quite easily. Although photodiodes have a potential detection bandwidth of many MHz, practical limits are set by the shot noise due to the finite number of photons detected per sample interval at reasonable laser powers and by electronic noise in the preamplifier (Denk and Webb, 1990; Gittes and Schmidt, 1997a,b). Fast detection avoids the low-pass filtering that is inherent in video imaging and that conceals details of molecular motions.

The approach we present here is to monitor, with a quadrant photodiode, shifts in the pattern of laser intensity in a plane exactly conjugate to the back-focal plane (BFP) of the condenser of our microscope. Laser light intensity shifts are caused by a refractive particle near the laser focus in the specimen plane. The technique works in parallel with optical trapping and has several unique properties: the displacement detection is biaxial, independent of the position of the laser focus in the specimen plane, and compatible with multiple-trap configurations. We derived a simple but quantitative model explaining the detection scheme as a far-field interference effect between the illuminating light and the light scattered by the trapped object. The model predicts the measured spatial response characteristics of the detector well. The detection method was used to investigate, with high temporal and spatial resolution, the path of beads driven by ncd-glutathione-S-transferase (GST) fusion proteins moving over the microtubule surface. Both axial and lateral motions were observed, and spectral analysis was used to probe the dynamics of the beads.

MATERIALS AND METHODS

Microscope design

Our custom-designed inverted microscope (Fig. 1 *A*) is constructed on an optical rail system (Newport Corp., Irvine, CA), mounted on a vibration isolating optical table (Technical Manufacturing Corp., Peabody, MA). The optical components are from Zeiss (Carl Zeiss, Thornwood, NY). The microscope is designed for trans-illumination DIC microscopy and epi-illumination fluorescence microscopy with simultaneous use of a laser as optical tweezers. For video imaging we use an Ultricon tube camera (VT1000, Dage-MTI, Michigan City, IN). For optical tweezers we use a CW diode pumped Nd:VO_4 laser (1.064 μm, 2W, Topaz 106C, Spectra Physics Lasers, Mountain View, CA). It was found to be important to guide the laser beam through tubes (Plexiglas) to prevent pointing fluctuations due to air currents and dust. An optical isolator (Optics for Research, Caldwell, NJ), providing 37 dB isolation against back reflections was necessary to keep the mode pattern of the laser stable. Mode jumps change the beam direction and intensity pattern sufficiently to contribute to noise in the displacement signal. Residual thermal beam pointing fluctuations

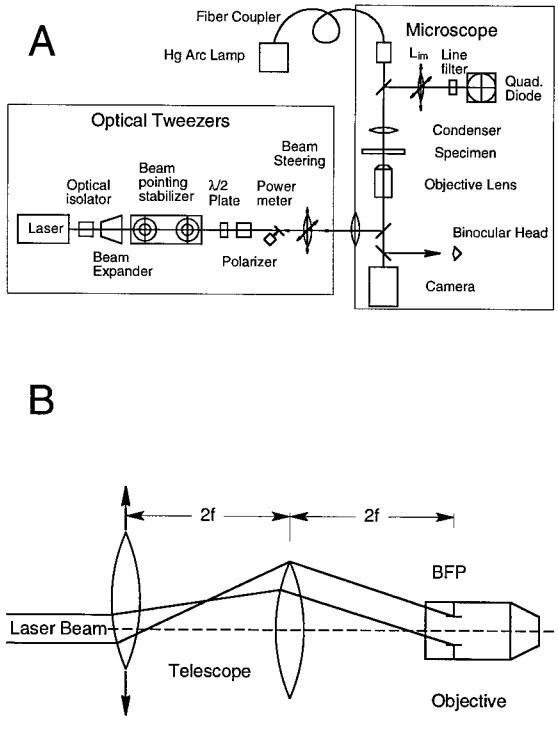

FIGURE 1 (*A*) Schematic diagram of custom microscope as described in the text. (*B*) Arrangement of two equal focal length lenses as a 1:1 telescope for beam steering as described in the text.

were a serious problem at frequencies below ~1 Hz, and therefore we have developed an active feedback controlled beam pointing stabilizer, which will be described elsewhere (unpublished). A 3× beam expander (CVI Laser Corp., Albuquerque, NM) was used to increase the width of the laser beam, reducing the size of the focus in the specimen plane as necessary to achieve trapping. The laser power in the specimen is controlled by a half-wave plate/polarizer combination, so that the laser itself can be run at relatively high power for stable operation.

A 1:1 telescope allows movement of the trap in the specimen plane (Fig. 1 *B*). The beam profile in the plane of the first lens is imaged by the second lens into the BFP of the objective. The image at the BFP remains stationary, but the angle of rays through that plane changes as the first lens is moved laterally to move the focus in the specimen plane. Consequently, the intensity distribution in the condenser BFP does not change with trap position. An angular change of 0.4° in the incoming beam causes a 10-μm displacement in the specimen plane. Laser light is coupled into the microscope optics via a dichroic mirror below the objective (×100, 1.3 NA; Neofluar, Zeiss). After passing through the sample, the beam is recollimated by an oil immersion condenser (1.4 NA; Zeiss), and a second dichroic mirror reflects the laser light out of the imaging path. An additional lens (F = 50 mm) images the condenser BFP through a laser line filter onto a quadrant photodiode (10-mm diameter, 10-μm gap; UDT Sensors, Hawthorne, CA) (Fig. 2 *A*). Proper imaging is controlled by replacing the quadrant diode with a CCD camera for alignment.

The two dichroic mirrors allow the simultaneous use of trans-illumination DIC microscopy using the 546-nm line from a mercury arc lamp. For DIC, a pair of Wollaston prisms are mounted below the objective and above the condenser. The laser beam is polarized such that it is not split by the Wollaston prisms and such that the laser light is S-polarized for the dichroics.

The signals from the quadrant diode are amplified by low-noise preamplifiers, networked so that two and two quadrants are grouped for X and Y detection, respectively. The normalized differences are calculated by analog electronics for the X and Y signal, respectively, anti-alias filtered if desired, and read into an IBM-compatible PC via an A/D board (AT-MIO16X, National Instruments, Austin, TX) (Fig. 2 *B*). These differences are then a measure for the lateral displacement of the trapped particle in the plane normal to the optical axis with respect to the center of the trap. In the figures we give the relative difference between the light intensities I_+ and I_- on the respective halves of the quadrant diode, $(I_+ - I_-)/(I_+ + I_-)$, in percent, ranging from +100% to −100%. Motor motility data were usually not filtered against aliasing so as to obtain true samples of position (up to the 100-kHz bandwidth of the A/D converter) even when using a low sampling rate. Spectra calculated from these data must be understood to contain aliasing distortions, but the integral over the power spectral density will be correct (which is not the case for filtered data). The signals are displayed and stored using software written in Labview (National Instruments).

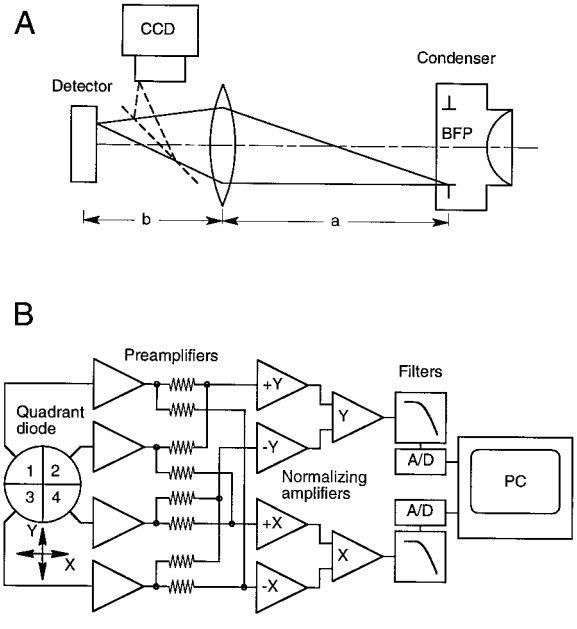

FIGURE 2 (*A*) Schematic diagram of displacement detection by imaging the back-focal plane (BFP) of the microscope condenser onto a quadrant photodiode. A lens of 50 mm focal length is placed such that the BFP of the condenser (~20 mm diameter) is imaged onto the 10-mm-diameter, circular quadrant photodiode. A mirror can be inserted so that the laser diffraction pattern in the BFP can be viewed with a video camera. (*B*) Analog and digital data processing as explained in the text.

Calibration of position detection

As our primary calibration method, beads were immobilized on a coverglass and positioned in the laser focus, and the entire stage was moved with piezoelectric actuators (P-775.00, Polytec PI, Auburn, MA) while the detector signal was recorded together with the driving voltage (Fig. 3 *A*). Producing an accurate triangular motion was complicated by the inherent hysteresis of the piezoelectric actuators. To compensate for this and to calibrate the piezos, video-recorded large-scale bead motion (viewed under

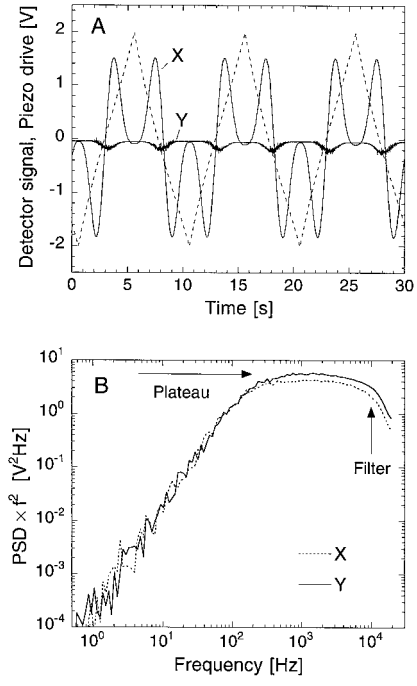

FIGURE 3 Quadrant diode response calibration. (*A*) Detector signals (X and Y, drawn lines) in response to the motion of a silica bead through the laser focus in the X direction. A 0.5-μm silica bead is fixed to a coverslip surface in a water-filled sample chamber. The microscope stage is moved by piezo electric actuators driven with a synthesized signal (- - -) to produce linear motion as described in the text. The amplitude of the motion was 2 μm, and the frequency was 0.1 Hz. (*B*) Power spectral density of the thermal fluctuations of a trapped 0.5-μm silica bead ~4 μm above the substrate surface, multiplied with the square of the frequency. The laser power in the specimen was ~14 mW, the beam diameter in the BFP of the objective ~2 mm. With the assumption of Stokes drag, and the knowledge of the bead size, the detector response can be calculated from the height of the plateau as described in the text. The effect of anti-alias filtering (at 20 kHz) is visible as a steep drop in the spectrum at the high-frequency end.

DIC) was analyzed by centroid tracking (Metamorph software, Universal Imaging Corp., West Chester, PA) and calibrated against a stage micrometer with 10-μm rulings. Hysteresis of the actuators was fitted to third-order polynomials and found to scale approximately with voltage. To drive the actuators in an accurate triangular motion, we digitally synthesized a proper waveform using the inverse to the hysteresis function and used this to produce up to ~5-μm peak-to-peak bead motion in each direction, typically at a frequency of 0.1 Hz.

Calibration curves, such as in Fig. 3 *A*, have an approximately linear range that increases with bead size; for 0.5-μm beads the response is roughly linear over $\pm$150 nm. From the slope of the calibration curve (in volts/second) and the known stage velocity, the detector response β in volts/nanometer can be calculated. The response is a function of bead size. For small beads, the response should be proportional to d^3; after passing through a maximum, the response should then decrease as $1/d$ for beads much larger than the laser wavelength (see Theory of detection, below). This behavior was experimentally observed (unpublished results).

As a convenient but indirect method of measuring detector response we analyze displacement fluctuations of optically trapped beads of known size. The power spectrum $S(f)$ of these fluctuations near the center of an optical trap is approximately Lorentzian (Svoboda and Block, 1994a; Gittes and Schmidt, 1997). Thus, if the bead has a diameter d in a solvent of viscosity η and κ is the trap stiffness, then the spectrum in units of distance^2/frequency is

$$S(f) = \frac{S_0 f_0^2}{f_0^2 + f^2}, \tag{1}$$

where f is the frequency, $S_0 = 4\gamma k_B T/\kappa^2$ is the zero-frequency intercept of $S(f)$, $f_0 = \kappa/2\pi\gamma$ is the corner frequency of the spectrum, and $\gamma = 3\pi\eta d$ is the Stokes drag coefficient of the bead. One can easily estimate detector sensitivity β from an uncalibrated voltage power spectrum, $S^V(f) = \beta^2 S(f)$, without knowing the stiffness of the trap, by multiplying the voltage power spectrum by f^2. The multiplied spectrum $f^2 S^V(f)$ reaches a plateau for $f \gg f_0$, as shown in Fig. 3 *B*, where the plateau value P^V can be measured and used to estimate the sensitivity β:

$$P^V = \beta^2 S_0 f_0^2 = \beta^2 \frac{k_B T}{3\pi^3 \eta d}.$$

$$\beta = (3\pi^3 \eta P^V d/k_B T)^{1/2} \approx (P^V d/5.0 \times 10^{-20} m^3/s)^{1/2} \tag{2}$$

This last formula applies to water at room temperature and gives β in units of volts/meter. We find this calibration method to agree with the active-displacement calibration, using piezo-actuated stage movement, typically within ~20% for the same size bead. The discrepancy may in part reflect a trapping position that is displaced (due to scattering forces) from the optical focus of the laser. The trap stiffness can be obtained independently of Eq. 2 by measuring the corner frequency of the spectrum, $f_0 = \kappa/2\pi\gamma$.

Proteins

Construction of pGEX-N195

Construction of pGEX-N195 was described previously (Stewart et al., 1993). The fusion protein encoded by pGEX-N195 contains GST, the pGEX-2T thrombin cleavage site, the sequence GPI from the polylinker, and amino acids 195–685 of ncd. This fusion protein, referred to as GST-N195, is similar to the GST-MC1 fusion protein described by Chandra et al. (1993). The GST-MC1 protein contains GST fused to amino acid 210 of ncd. The discrepancy in the numbering of amino acids is due to the choice of the start codon in the cDNA. In our numbering scheme, using the second ATG in the ncd cDNA as the initiator codon, amino acid 195 is the lysine residue encoded by the unique *Afl*II restriction site of ncd. In the numbering scheme used by Chandra et al. (1993), which uses the first ATG in the ncd cDNA as the initiator, amino acid 210 is the lysine residue encoded by the unique *Afl*II site.

Purification of motor proteins and tubulin

GST-N195 was affinity purified from *Escherichia coli* using glutathione-agarose, as described previously (Stewart et al., 1993). Briefly, GST-N195 expression was induced by the addition of 0.1 mM isopropyl β-D-thiogalactopyranoside in approximately mid-log cultures of *E. coli*, which were then shaken at 20–22°C for an additional 4–6 h. After harvesting the cells by centrifugation, they were resuspended in lysis buffer (20 mM PO_4, 1 mM EDTA, 150 mM NaCl, pH 7.2) and lysed by sonication. The lysate was clarified by centrifugation (17,000 rpm, Beckman JA-17 rotor). Glutathione-agarose beads (Sigma Chemical Co., St. Louis, MO) were added to the lysate. After mixing at 4°C for 30–60 min, the beads were washed extensively with PEM80 buffer (80 mM Pipes, 1 mM EGTA, 4 mM Mg^{2+}, pH 6.9). GST-N195 was then eluted with 10 mM glutathione in PEM80. GST-N195 was frozen in liquid N_2 in small aliquots and stored at −80°C. The protein concentration was ~0.7 mg/ml.

Tubulin was purified from bovine brain following standard recipes (Williams and Lee, 1982). Aliquots were frozen in liquid N_2 and stored at −80°C. The protein concentration was ~3.0 mg/ml (Bio-Rad Protein Assay, Bio-Rad Laboratories, Hercules, CA).

Motility assays

Preparation of proteins

Unless noted, all reagents were from Sigma Chemical Co. or Fisher Scientific (Pittsburgh, PA). Tubulin was thawed, polymerized with 1 mM GTP at 37°C for 30 min, and diluted 10-fold into PEM40 (40 mM Pipes, 0.5 mM EGTA, 1 mM Mg^{2+}, 1 mM NaN_3) containing 10 μM taxol. For some experiments, the polymerized microtubules were further centrifuged (135,000 × *g*; Airfuge Ultracentrifuge, Beckman Instruments, Fullerton, CA) to separate microtubules from unpolymerized tubulin. The supernatant was discarded and the pellet was gently resuspended in the original volume of PEM40 with 10 μM taxol. In both cases, microtubules were kept at room temperature, protected from light, and used in experiments for up to 3 days. GST-N195 aliquots were rapidly thawed and brought to 50 mM dithiothreitol. For some experiments, the protein was further centrifuged (135,000 × *g*; Airfuge Ultracentrifuge) to remove protein aggregates, and the top 80% of the supernatant was recovered. In both cases, the GST-N195 was kept on ice and used in experiments for up to 10 h.

Preparation of GST-N195-coated beads

Silica beads of 0.5 μm diameter (a kind gift from E. Matijewic) were transferred by repeated centrifugation (four times at 16,000 × *g*; Eppendorf Microcentrifuge, Brinkmann Instruments, Westbury, NY) into anhydrous ethanol and coated by incubation in a 2% v/v solution of Sigmacote (Sigma) in anhydrous ethanol. After another centrifugation step to remove unreacted Sigmacote, the pellet was resuspended in anhydrous ethanol and probe sonicated (Sonifier Cell Disruptor, Branson Ultrasonics Corp., Danbury, CT) to break up bead aggregates. The Sigmacote beads were incubated with GST-N195 on ice for ~5 min at final concentrations of 1.4×10^{10} ml^{-1} beads and 7, 1.4, and 0.7 μg/ml protein. The motility assay buffer (AB) consisted of vacuum-degassed PEM40 with an added oxygen-scavenging system, blocking protein and nucleotide (0.018 mg/ml catalase, 3 mg/ml glucose, 0.1 mg/ml glucose oxidase, 0.1 mg/ml casein, 10 μM taxol, 50 mM dithiothreitol, and 1 mM of either MgATP or Mg Adenylylimidodiphosphate (AMP-PNP)). At the protein dilutions we used, multiple motors were expected to be bound to each bead. Assuming, as an upper limit, that all motors in solution adsorbed to the beads, we estimate 2200, 450, and 220 motor dimers per bead for the three dilutions. However, only a fraction of this number may be bound to a bead, and some of the bound motors are possibly inactive.

Assembly of the sample chamber

Motility assays were performed in flow chambers assembled from two coverglasses and narrow strips of double-stick tape (Scotchbrand, 3M, St.

Paul, MN) that were then attached to stainless steel holders for mounting on the microscope stage. KOH/ethanol-cleaned coverglasses were silanized with trimethoxysilylpropyl-diethylenetriamine (DETA, United Chemical Technologies, Bristol, PA) as described previously (Fritz et al., 1995) to provide a positively charged surface to which microtubules strongly attach. Precleaned coverslips were immersed for 5 min in a 1% solution of DETA in 1 mM acetic acid, cleaned by bath sonication for 2 min in a large volume of deionized water, and then dried and cured in an oven at 150°C for 15 min. The chamber was filled with 20 μl of a 1:100 dilution of the microtubule stock solution. After allowing the microtubules to adsorb to the surface for ~2 min, the chamber was flushed with AB buffer containing 1 mg/ml filtered casein. Finally, GST-N195 beads, diluted 1:1000 in AB buffer, were pipetted into the chamber.

Individual beads were captured in solution with the optical tweezers and brought in contact with immobilized microtubules while their motion was monitored with the quadrant diode detector. In the case of bound beads (with AMP-PNP) the motion was purely thermal; with ATP the motion is partly thermal and partly motor driven. Data were digitized at a scan rate of 2 kHz, without any filtering so that the full range of displacements was sampled. Binding and motility of beads on microtubules were also observed with video-enhanced DIC microscopy and recorded on videotape. When the microtubule was not parallel to a detection axis, the X and Y data were rotated (by an angle measured from video) to resolve axial and lateral motion. Such a rotation is meaningful only near the focus center, however, where the detector response is approximately linear.

Video tracks of moving beads were constructed by centroid tracking (Metamorph software, Universal Imaging) to compare with the detector data. The 30-Hz video track was interpolated and the 2-kHz detector data were filtered to a common sample interval; the data were then aligned so as to minimize their mean squared difference.

Theory of detection

Laser trapping has been modeled quantitatively for large particles in a ray optics regime (Ashkin, 1992; Gauthier and Wallace, 1995). When we observe the laser intensity in the condenser BFP with a smaller-than-wave length bead in the vicinity of the laser focus, diffraction and interference, which can not be described by ray optics, appear to be the most prominent effects. Theoretical treatments using rather complicated series expansions have been developed to obtain precise estimates of forces in relatively low-angle Gaussian beams (Gouesbet and Lock, 1994; Lock and Gouesbet, 1994; Harada and Asakura, 1996); however, these do not provide a simple explanation of the far-field intensity. An accessible physical picture, describing how the laser intensity distribution in the BFP depends on experimental parameters, and how it can be used for displacement detection, is highly desirable.

We find that intensity changes in the BFP are quantitatively explicable as an effect of simple interference that occurs throughout the angular range of the focus (in contrast to plane-wave scattering problems (Hulst, 1957) where interference occurs only at zero angle).

The quadrant photodiode in our setup monitors the pattern of laser intensity in the back focal plane (BFP) of the condenser. As the laser enters the sample through the objective, the condenser acts as the imaging lens for the laser focus (see Fig. 1 *A*). Within ray optics, positional information about the specimen plane is hidden in the BFP. Even within wave optics, the BFP intensity is independent of lateral motion of the focus in the specimen plane, so that one can reposition the trap containing a bead without changing the BFP intensity pattern, apart from nonideality of the optics. The pattern in the BFP represents the angular distribution of light that has passed through the specimen, and thus measuring the BFP intensity distribution is equivalent to an angular scattering experiment. Furthermore, the momentum carried by the scattered light provides the lateral trapping force; in particular, the detection theory discussed here is closely connected with the gradient force exerted by the trap (Gittes and Schmidt, 1998).

For a well corrected lens of focal length f, light at a radius R in the BFP must have emerged from the focus at an angle θ, where $R = f \sin\theta$ (the sine condition (Born and Wolf, 1989)). We describe the direction of light in the far field by the angle θ from the optical axis and the azimuthal angle ϕ about this axis. This light will be understood to be detected in the BFP at a radius $R = f \sin\theta$ (and at the angle ϕ).

To predict the BFP signal caused by a bead in the vicinity of the laser focus, we need to derive the change in angular intensity distribution that occurs for a given displacement of a bead away from the focus. To attribute this intensity change to interference of scattered light with the original beam, we need a description of the scatterer and the incoming light field. We make the following simplifications.

1) We are concerned with detecting beads that are smaller than or comparable to the wavelength of light. We replace our bead by a Rayleigh scatterer, i.e., a point-like polarizable object. This approximation is not too drastic because we use the uniform-field polarizability α corresponding to our actual sphere radius (Eq. 5, below). In effect, we take the incoming laser field to be uniform over the volume of this sphere.

2) We describe the focus itself in a small-angle (paraxial) approximation, where $\sin\theta \approx \tan\theta \approx \theta$. This is a substantial simplification because the polarization of the light drops out of the problem (Born and Wolf, 1989). If the optical axis is defined as the z direction, we can, for example, take the electric field of the light to point in the x direction everywhere, $E = E_x$. The laser intensity profile is approximately Gaussian with an estimated $1/e^2$ radius of $w_{in} \approx 1.0$ mm at the objective BFP, corresponding to a half-angle of ~30° at the focus (assuming an objective focal length of ~2.1 mm, and $n = 1.33$ in the specimen). At 30°, $\tan\theta/\theta \approx 1.1$ and a paraxial approximation is reasonable. The paraxial approximation also allows for simple and well known expressions for small-angle Gaussian beams (Siegman, 1986). Larger-angle electromagnetic vector solutions to focused Gaussian beams are also available (Yoshida and Asakura, 1974; Axelrod, 1989); however, these are not necessary for the present discussion.

Our model is sketched in Fig. 4 *A*. Light is focused at the origin ($\vec{r} = 0$). The customary formalism is that the actual electric field E of the light is the real part of a complex wave: $E = \mathrm{Re}\,\{\hat{E}\}$; time dependence is implicit, in a factor $e^{-i\omega t}$ that is not shown. We observe outgoing light far from the focus, at an angle θ from the optical axis. Using SI electromagnetic units and manipulating formulas for a simple Gaussian beam (Siegman, 1986) the diverging wave far from the focus is

$$\hat{E}(\vec{r}) \approx \frac{-ikw}{r\sqrt{\pi\epsilon_s c_s}} \exp\left\{ikr - \frac{1}{4}k^2w^2\theta^2\right\}, \quad (r \gg w). \qquad (3)$$

For the same beam, the field in the focal plane, at a lateral displacement x, is

$$\hat{E}(\vec{r}_s) = \hat{E}(x) = \frac{2}{w\sqrt{\pi\epsilon_s c_s}} e^{-x^2/w^2} \quad \text{(focal plane)}. \qquad (4)$$

Here $k = 2\pi n_s/\lambda$, where $\lambda = 1.064$ μm is the vacuum wavelength of the light, ϵ_s and n_s are the permittivity and refractive index of the solvent, respectively, c_s is the speed of light in the solvent, and w is the beam half-waist in the focus (the $1/e$ radius of field, not intensity). Equations 3 and 4 are normalized to give the beam a total dimensionless power of 1. Suppose a small sphere of diameter d is displaced laterally by x in the focal plane, which we denote also by the vector $\vec{r}_s$. The particle will have an induced dipole moment $p = 4\pi\epsilon\alpha E$ where α is the electric susceptibility (this particular definition is convenient here). For a sphere with an index of refraction relative to the solvent of $n_r = n/n_s$, the susceptibility is (Jackson, 1975)

$$\alpha = (d/2)^3 \frac{n_r^2 - 1}{n_r^2 + 2}. \qquad (5)$$

This comes out to $\alpha \cong 0.0074\, d^3$ if we assume $n = 1.45$ for silica beads (Lide, 1992) and $n = 1.33$ for an aqueous solution (Hale and Querry, 1973), both at 1.064 μm wavelength. In the Rayleigh approximation the

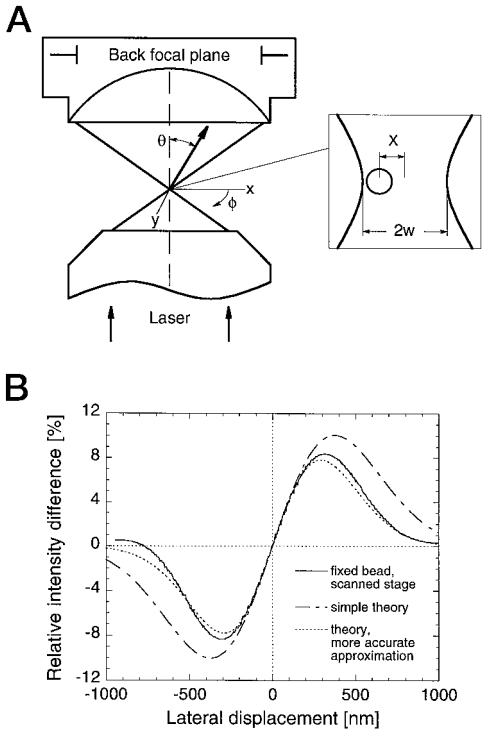

FIGURE 4 (*A*) Diagram indicating the geometry discussed in the text, for interference observed in the back focal plane of the condenser lens between an unscattered Gaussian beam and scattered light from a refractive object located in the focal plane of the beam. For emerging light far from the focus, θ is the angle from the optical axis and ϕ the azimuthal angle about the optical axis. The angular size of the Gaussian beam, ~30° in our experiments, is here exaggerated. The inset shows the focal region with a laterally displaced bead. (*B*) The experimental calibration (drawn line) is compared with the simple theory presented in this paper, as well as with an improved calculation presented elsewhere (Gittes and Schmidt, 1998). Both theoretical curves contain no adjustable parameters but depend strongly on the nominal bead diameter of $d = 0.5$ μm and a waist radius $w = 0.53$ μm estimated from the radius of the input beam before the objective.

local electric field $\hat{E}(x)$ acting upon this dipole gives, at large r, a scattered field

$$\hat{E}'(\vec{r}) \approx \frac{k^2\alpha}{r}\hat{E}(x)\exp(ik|\vec{r}-\vec{r}_s|) \approx \frac{k^2\alpha}{r}\hat{E}(x)\exp ik[r - x\sin\theta\cos\phi], \quad (6)$$

where θ and ϕ are the angles of observation. The total field far away is $(\hat{E} + \hat{E}')e^{-i\omega t}$ (including the implicit time factor), the sum of the unscattered beam in Eq. 3 and the scattered field in Eq. 6. The time-averaged squared real part of this is $|\hat{E} + \hat{E}'|^2/2$. Therefore, the change in time-averaged light intensity I, due to the interference between the laser beam and the scattered light is

$$\delta I = \frac{\epsilon_s c_s}{2}\{|\hat{E}+\hat{E}'|^2 - |\hat{E}|^2\} \approx \epsilon_s c_s \mathrm{Re}\{\hat{E}\hat{E}'^*\}. \quad (7)$$

A term $|\hat{E}'|^2$ was discarded; as a result, Eq. 7 represents simple first-order interference. Substituting Eqs. 3, 6, and 4 into Eq. 7 and making a small-θ approximation ($\sin[kx\sin\theta\cos\phi] \cong kx\theta\cos\phi$) gives for the intensity change

$$\frac{\delta I(x)}{I_{tot}} \cong \frac{2k^4\alpha}{\pi r^2} x e^{-x^2/w^2}\theta\cos\phi\, e^{-k^2w^2\theta^2/4}. \quad (8)$$

Equation 8 describes the pattern of intensity modulation caused by a particle displaced by x from the optical axis in the focal plane, observed in the direction (θ, ϕ). Because of the $\cos\phi$ factor, this intensity change consists of a negative lobe on one side of the BFP and a positive lobe on the other, both proportional to x. This means that detection is efficiently performed by simply taking the difference in total power between the two halves of the BFP. Suppose a split diode is oriented with its plus and minus halves along the $\pm x$ axis. The signal change on the plus half (i.e., $-\pi/2 < \phi < \pi/2$) is

$$\frac{\delta I_+}{I_{tot}} \cong r^2\int_{-\pi/2}^{\pi/2} d\phi \int_0^{\theta_{max}} d\theta \sin\theta\, \delta I(x) \quad (9)$$

The signal change on the plus and minus halves are equal and opposite: $\delta I_- = -\delta I_+$. We can take $\theta_{max} = \infty$ because $\delta I(x)$ in Eq. 8 is cut off strongly in θ by the exponential factor. Putting Eq. 8 into Eq. 9 (again with $\sin\theta \cong \theta$) and integrating gives

$$\frac{(I_+ - I_-)}{(I_+ + I_-)} \cong \frac{16}{\sqrt{\pi}}\frac{k\alpha}{w^2}(x/w)e^{-(x/w)^2}. \quad (10)$$

This formula predicts the absolute detector response, as a function of the diameters of the particle and the focus. It is remarkably simple. In Fig. 4 *B*, the prediction of Eq. 10 is compared with an actual calibration (the same one as shown in Fig. 3 *A*). We assume simply the nominal sphere size ($d = 0.5$ μm) and a focus size roughly estimated from the input beam width. For the latter, we assume that the beam enters the microscope with an intensity profile of $\exp(-2R^2/w_{in}^2)$ where, from beam-width measurements, $w_{in} \approx 1.0$ mm and. Using $f \approx 2.1$ mm, a basic relationship between angular divergence and focal waist diameters for Gaussian beams (Siegman, 1986) is $kw \approx 2f/w_{in}$, implying $w = 0.53$ μm. The resulting theoretical curve is similar in range and shape to the measured response curve, notably including its slope in the linear region, despite the lack of adjustable parameters. It is also possible to evaluate a more complicated integral for the intensity imbalance without making the approximation $\sin[kx\sin\theta\cos\phi] \cong kx\theta\cos\phi$ above Eq. 8 (Gittes and Schmidt, 1998), and we include this curve in Fig. 4 *B* to give an idea of the uncertainty in Eq. 10.

As the waist radius w is of the order of λ, the slope of the linear region of Eq. 10 is proportional to $d^3/\lambda w^3 \approx d^3/\lambda^4$. A cubic dependence will arise in all theories based on Rayleigh scattering; it applies to beads somewhat smaller than the wavelength of light, but not necessarily much smaller, as our model works well for spheres a half-wavelength in diameter. For beads much larger than the wavelength of the laser, ray optics become applicable and the wavelength drops out of the problem. Then the bead size is the only relevant length scale and detection can only be a function of x/d. Consequently, the response must decrease as $1/d$ for very large beads.

Control experiments

Fig. 5 demonstrates the sensitivity of the displacement detection. The detector signal was balanced to zero in the X and Y directions by laterally adjusting the lens that images the condenser BFP (L_i in Fig. 1 *A*), without an object in the trap. A silica bead of 0.5 μm diameter, fixed on a glass slide, was then centered in the laser trap by moving the microscope stage with piezo actuators until the detector signal was zeroed again. Then the stage with the bead was moved in a sinusoidal fashion. At a peak-to-peak amplitude of 30 Å the detector signal clearly monitored the bead displacement, both in the X and in the Y direction. At a laser power of ~10 mW in the specimen plane, the noise limitation did not stem from photon shot noise but mainly from acoustic noise in the microscope and from beam instabilities. A narrow-band signal like the sinusoidal stage motion could of

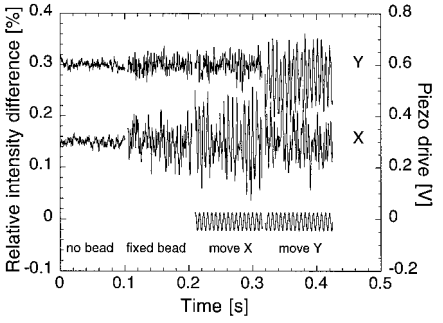

FIGURE 5 Sensitivity of quadrant diode displacement detection. The laser power is 12 mW, the objective BFP is overfilled by inserting an additional beam expander immediately in front of the first telescope lens, and data were digitized at 4 kHz and anti-alias filtered at 2 kHz. The response is plotted as a relative difference between the signals on the two respective halves of the quadrant diode $(I_+ - I_-)/(I_+ + I_-)$, for comparison with Figs. 4 *B*, 8, and 12 (left ordinate). The piezo driving voltage is labeled on the right ordinate). From left to right is shown 1) noise signal without a bead in the laser focus, 2) noise signal with 0.5-μm silica bead laterally centered in the laser focus and adjusted in the axial direction for maximal detector sensitivity, 3) response in X and Y channel to a 30-Å peak-to-peak sinusoidal stage motion in the X direction, and 4) same with 30-Å motion in the Y direction.

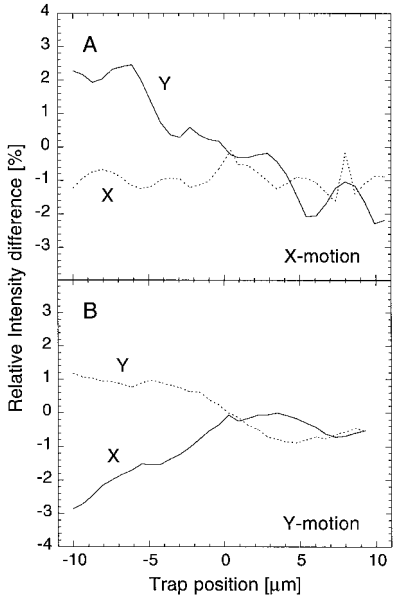

FIGURE 6 Sensitivity of position detection to motion of the trap across the microscope field of view within ± 10 μm in X and Y directions (signal balanced in the center of the field of view). For this experiment, no bead is trapped in the laser focus. (*A*) Relative change of the light intensity balance between the X and Y halves of the quadrant diode when moving the trap in the X direction. (*B*) Same as *A* but moving in the Y direction.

course be extracted from the power spectrum of the signal, even if it is not visible in the direct time series data. However, when detecting nonperiodic motion, a common experimental situation with motor proteins, the broad-band noise floor evident in Fig. 5 is more relevant. The signal-to-noise ratio can in principle be improved by low-pass filtering the data above the highest frequency of interest, thereby rejecting high frequency noise contributions (Gittes and Schmidt, 1997a,b), but in our case a substantial part of the noise is from acoustic vibrations of the instrument at relatively low frequencies.

Ideally, displacement detection, being relative to the trap, would be insensitive to repositioning of the trap in the field of view. In practice, a DC offset is generated in the displacement signal by moving the trap in the field of view, as shown in Fig. 6. Without a bead in the laser focus, the detector signal is zeroed with the trap in the center of the field of view and the focus close to the substrate surface. The trap is then moved in increments of ~ 1 μm for a total of ± 10 μm in the X and in the Y direction by moving the first telescope lens as explained in Fig. 1 *B*. The resulting detector signal is given as relative change in the signals from the two respective halves of the quadrant detector compared with the average intensity. For the roughly 20-μm-large field of view, the relative change in the signal is less than 3%. This remaining variation is probably due to less than perfect alignment of the beam-steering lenses and the detector, as well as to contaminations on the optical elements, especially the first telescope lens, which is imaged onto the detector. In practice, the trap can therefore be moved in the specimen without losing AC sensitivity, but a substantial change in the DC offset of the signal has to be taken into account. To give a basis for comparison, the signal of 3% would correspond to a 90-nm displacement of a 0.5-μm bead.

RESULTS

In ATP buffer, at the three concentrations of ncd motor used, a variable fraction of the beads in the sample moved along microtubules. Nonspecific adhesion to the substrate was a persistent phenomenon, even in the presence of 1 mg/ml casein blocking protein. Fig. 7 shows three video frames of a bead moving through the stationary laser focus. For these experiments the number of motors per bead interacting simultaneously with a microtubule was not determined. The stoichiometry is 200-2000 ncd dimers per bead (see Materials and Methods), but only a fraction of these are expected to be functional. At the lowest motor density, we observed occasional motility, but beads were contained within the relatively weak trap ($\sim 4.5 \times 10^{-3}$ pN/nm). At <450 and <2000 motors per bead, motility was more consistent and the velocity of the beads was determined from the video recordings as 230 ± 30 nm/s. Fig. 8 shows axial displacements measured at high resolution with the quadrant detector for two events such as the one shown in Fig. 7, for a weak ($\sim 4.5 \times 10^{-3}$ pN/nm) and a very weak ($\sim 2 \times 10^{-3}$ pN/nm) trap. Microtubules were not generally aligned with an axis of the detector; therefore, data sets were rotated as described in Materials and Methods. Entering the focus, beads were first pulled forward, which constitutes a negative load; near the center the load decreases to zero and then becomes positive. A zero-load interval is evident as a pause in the track for the stronger trap: attachments apparently remain slack as the motors move from a lagging to an advanced position. Although even the strong trap is relatively weak (maximal force ≤ 0.7 pN) the bead velocity decreased slightly under positive load (163 ± 56 nm/s) as clearly seen in Fig. 8.

Two-dimensional high-resolution detection reveals both axial and lateral displacements of the bead over the microtubule. Lateral thermal displacements might be constrained by multiple attachment points as well as by intrinsic rigidity of the attachments themselves (Wang et al. 1995), and if constrained enough, the path the motors take over the microtubule surface should become visible. Optical trapping, on the other hand, also decreases lateral excursions as can be seen

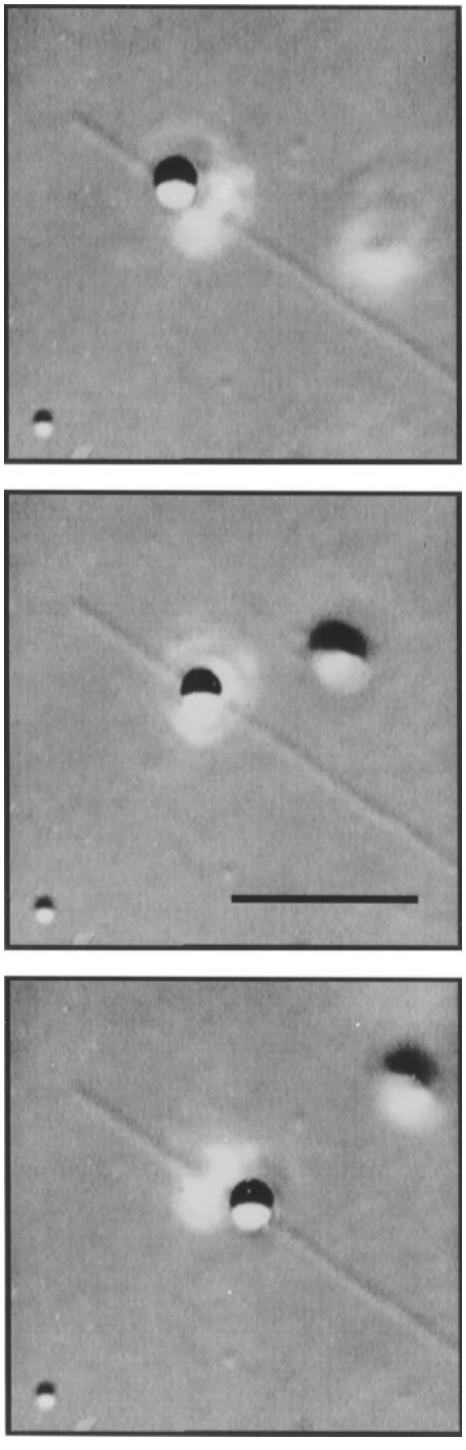

FIGURE 7 Video frames (0, 7.5, and 15 s) of a 0.5-μm silica bead driven by multiple ncd motors through a stationary trap/detector along a microtubule immobilized on a silanized glass substrate. The laser power was 12 mW in the specimen. Scale bar, 5 μm.

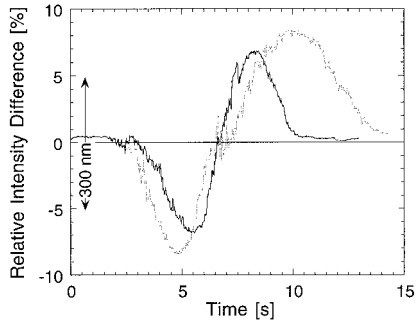

FIGURE 8 Quadrant detector signals from ncd-driven beads traveling through the laser focus, taken at different laser powers and trap stiffnesses. Plotted are the relative intensity differences on the detector versus time. For the gray line, laser power was 12 mW and trap stiffness was 4.5×10^{-3} pN/nm. For the black line, laser power was 4.4 mW and trap stiffness was 2×10^{-3} pN/nm. Data for both tracks were rotated as the microtubules were oriented at 54.7° (high power) and 87° (low power) to the x axis, respectively. Therefore, the fringe regions (outside of the marked interval) of the displacement data are distorted (especially for the high-power track). These data (unlike the ones in Fig. 10) were smoothed using a Savitsky-Goley filter (Press et al., 1992) with a window size of 50 points.

in the video track of Fig. 9. Video tracking alone does not provide sufficient information, because the effective low-pass filtering conceals the true excursions of the bead. Fig. 10 *A* shows a video track together with the simultaneous quadrant detector signal, sampled at 2 kHz but unfiltered out to ~100 kHz (a limit due to the sample and hold circuitry of the A/D conversion board). The full lateral range of motion estimated from the time series data was ~210 nm in the weakest trap and ~200 nm for the stronger trap. The track width outside the focus, estimated from video (Fig. 9) appears as ~260 nm but, because of low-pass filtering, may be underestimated by a factor of 2 (Fig. 10 *A*).

Control beads were prepared identically but with ATP replaced by AMP-PNP. Beads bound to microtubules but sometimes also to the substrate surface at all the motor dilutions used. This made the binding eventually irreversible, even after adding an excess of ATP. Therefore, the results are not reliable with respect to the motor attachment compliance.

A strongly limited lateral motion might have been expected if the motors were protofilament tracking, such as kinesins (Berliner et al., 1995). However, the lateral displacement shown in Fig. 9 from video analysis (low-pass filtered) and in Fig. 10 *A* from interferometric detection

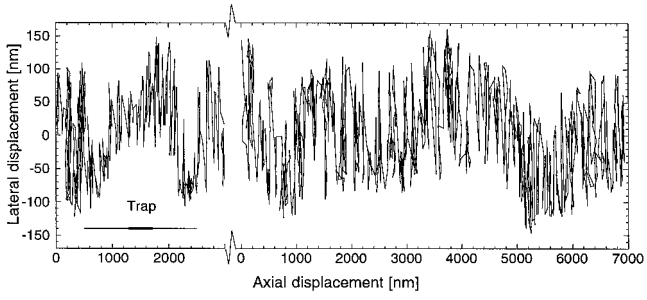

FIGURE 9 Spatial track of ncd-driven 0.5 μm silica bead detected by video centroid tracking, before, while and after passing through the laser focus (laser power 4.4 mW in the specimen, 2×10^{-3} pN/nm trap stiffness). Note the expanded scale in the lateral direction. The horizontal line denotes the extension of the trap between the force maxima, the bar denotes the linear regime. Shown in continuation is the track followed by the same bead while moving along the microtubule with the laser switched off.

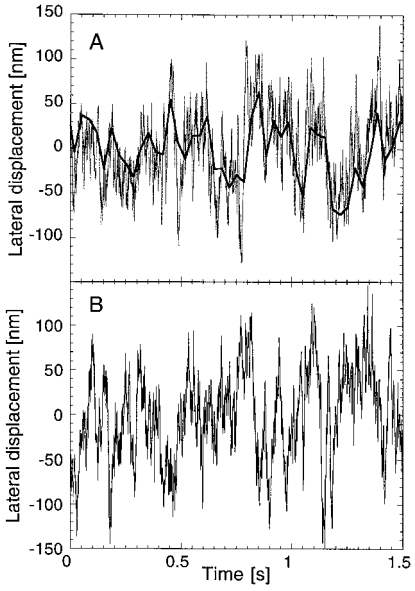

FIGURE 10 (*A*) Lateral motion of an ncd-driven 0.5-μm silica bead with respect to the microtubule axis, from quadrant diode detection and video tracking (laser power, 4.4 mW in the specimen; trap stiffness, 2×10^{-3} pN/nm; digitization rate, 2 kHz). The part of the track within the linear range of the detector is shown. Video and quadrant diode tracks were aligned along the time axis first roughly by eye and then more finely by searching for the minimum of the variance of the differences between the video track and a low-pass-filtered version of the quadrant diode signal. (*B*) Simulated track using a program based on a Gaussian random number generator (Press et al., 1992) but with correlations introduced. The two parameters (variance and correlation time) of the correlated Brownian motion were taken from the fit to the data in Fig. 11.

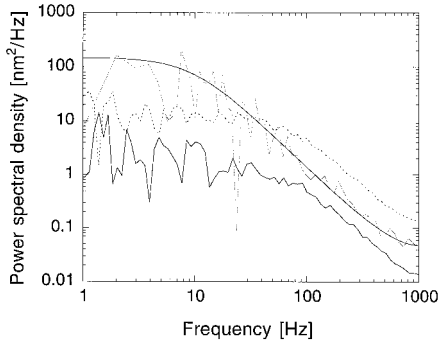

FIGURE 11 Spectral analysis of the lateral motion of an ncd-driven, a stationary (bound with AMP-PNP), and an unbound 0.5-μm silica bead. Single-sided power spectra were calculated from time series data of 1.5 s length, windowed with a Welch window, and smoothed by averaging in equally sized bins in the log domain. The data were not anti-alias filtered during recording to preserve high bandwidth displacement sampling. - - -, unbound bead trapped 1.4 μm above the substrate surface; ——, ncd-coated bead immobilized on a microtubule by AMP-PNP; gray line, ncd-coated moving bead. The drawn smooth line is the theoretical spectrum from which the simulated data track in Fig. 10 *B* is derived. Aliasing is included, producing the slight upward trend at the end of the spectrum.

shows no obvious constraint due to motor attachments. From visual inspection it is tempting to interpret the tracks as a relatively slow meandering of the motors over the accessible microtubule surface. On the other hand, this apparent lateral freedom could be a result of very flexible coupling of the beads. To demonstrate that it is possible to quantitatively test the motion by using the high bandwidth displacement data, we compared AMP-PNP-bound stationary beads with moving beads, and we analyzed the power spectra of the lateral displacement signals for both cases and compared with unbound beads away from the surface. We first visually compared the signal measured from the moving beads with simulated pure Brownian motion. Fig. 10 *B* shows a simulated displacement time series for Brownian motion in a harmonic potential with parameters chosen to produce data with similar spectral properties (amplitude and corner frequency) as observed for the ncd-driven bead (Fig. 10 *A*). The correlation time of this synthetic track $1/(2\pi f_0)$ is 0.023 s. Naive inspection of the data can be deceptive, as the eye suggests much longer dwell times than this correlation time. Fig. 11 compares power spectral densities calculated from time series positional data for unbound, ncd-driven and stationary beads (bound with AMP-PNP to the microtubule). The unbound bead has a Lorentzian power spectrum as expected (Eq. 1) with a corner frequency of $f_0 \approx 60$ Hz determined by the laser trap stiffness ($\sim 2 \times 10^{-3}$ pN/nm). The spectrum of the ncd-driven bead is also well fit by an aliased Lorentzian (taking into account the lack of anti-alias filtering) with a corner frequency $f_0 \approx 7$ Hz. The parameters used to produce the synthetic track in Fig. 10 *B* were obtained from this fit. The decreasing, high-frequency part of both the ncd-driven and stationary bead spectra has a log-log slope of -2. This reflects purely diffusive motion in the local viscous environment of the beads (e.g., the $\kappa = 0$ limit of Eq. 1 is $S(f) = k_B T/(\gamma \pi^2 f^2)$, independent of binding or motor interaction. The amplitudes of the ncd-driven and stationary bead spectra are both strongly decreased at high frequencies by factors of $\sim$3.5 and 10, respectively. This implies that the ncd-driven and stationary beads experience a viscous drag 3.5 and 10 times larger than that of the unbound bead. With the viscous drag known from the high-frequency part of the spectra, the constraint compliances can be deduced from the corner frequency of the power spectral density, as $f_0 \propto \kappa/\gamma$. For the ncd-driven bead the corner frequency decreased by roughly the same factor as the viscous drag increased, although the time series for the moving beads were not long enough to get a precise value for the corner frequency. The results nevertheless imply that there is no large effect of the motor attachments on the elastic constraint of the bead. In contrast, the AMP-PNP-bound bead shows an increased attachment stiffness.

In several cases a motile bead could not escape from the trap before releasing from the microtubule, and repeated escape attempts could be observed as shown in Fig. 12. This behavior may have been due to an especially small number of functional motors on a bead. The linear range of the detector for the 0.5-μm beads is approximately $\pm$150 nm. Around the maximum in the response signal, the signal becomes ambiguous and the resolution goes to zero. Therefore, instead of calculating the actual displacement with the

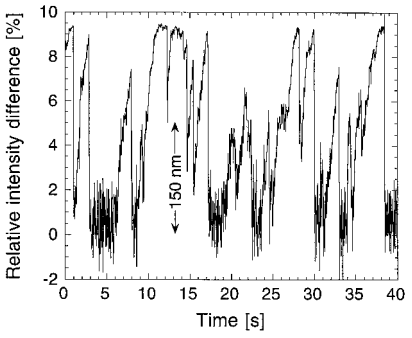

FIGURE 12 Repeated attempts of an ncd-coated 0.5-μm silica bead to escape from the trap (laser power, 12 mW; trap stiffness, 4.5×10^{-3} pN/nm). Plotted is the relative intensity difference on the detector versus time. The microtubule was oriented horizontally, and only the axial signal is shown. For the linear range, the scale in nanometers is given on the right.

help of the calibration curves (Fig. 3), in Fig. 12 we label only the linear part of the position detector range with a displacement scale.

DISCUSSION

We present a high-resolution displacement detection technique for molecular-scale motion, in conjunction with optical trapping, in a light microscope. We provide a simple but quantitative physical model of how a small refractive object near the focus of a laser affects through interference the intensity pattern in the back focal plane (BFP) of the condenser lens collecting the laser light. This picture complements earlier models treating the ray optics regime of large trapped particles (Ashkin, 1992) and is relevant to a practical understanding of laser trapping in general. We draw upon a paraxial Gaussian-beam approximation and well known scattering theory; the unusual feature is that, over the full range of outgoing angles, intensity change is due to a first-order interference effect. More rigorous electromagnetic treatments of spheres near foci (Barton and Alexander, 1989; Barton et al., 1989; Gouesbet and Lock, 1994; Lock and Gouesbet, 1994; Harada and Asakura, 1996) could in principle be extended to this problem, but our simpler model evidently captures the physical mechanism of detection and its dependence on experimental parameters. The model is applicable to related detection techniques that have been developed recently (Ghislain and Webb, 1993; Ghislain et al., 1994; Smith et al., 1996; Visscher et al., 1996).

Experimental detection accuracy was found to be on the order of a nanometer, using 0.5-μm silica beads as probes. Such beads are often used in optical trapping experiments, because they can be coupled to the molecules of interest, such as motor proteins, for micromanipulation. Technically, the BFP method is convenient to implement; it uses less complicated optics than split-beam interferometry and it works well for pure phase objects. Detection is biaxial, and minimal detector realignment is necessary when the laser focus is moved in the specimen plane. It can be used with double-trap arrangements where two beams are separated by polarization. In comparison with split-beam interferometry (Denk and Webb, 1990; Svoboda et al., 1993), BFP detection is of comparable sensitivity, but it is more susceptible to acoustic vibrations and thermal creep in the instrument as absolute shifts in the BFP intensity pattern are measured; the laser beam cannot be allowed to wander either in the specimen plane or in the BFP.

In exploratory experiments, we have applied BFP detection to the movement of ncd-coated beads along microtubules, where we find several experimental advantages compared with video tracking or uniaxial detection. 1) The high time resolution allows us to detect the position of a tethered bead typically faster than its thermal correlation time, which is the characteristic time it takes to explore its full range of motion. The effective low-pass filtering of video detection of motor tethered beads usually averages over many correlation times (Fig. 10 *A*). 2) The high time resolution makes spectral analysis possible. 3) With the bead bound to an immobilized track, measurement and control of axial and off-axis load is possible; experiments with kinesin (Gittes et al., 1996) have provided evidence for the importance of the load direction and have left open questions. 4) Off-axis motion can be detected and correlated with axial motion. Several studies using video microscopy have focused on the meandering track of motor proteins, dyneins (Wang et al., 1995), and single-headed kinesins (Berliner et al., 1995). These results have been difficult to interpret due especially to the low time resolution of video.

The motility experiments with ncd-coated beads show several conspicuous differences from the kinesin results. Even with multiple motors attached to a single bead, at our lowest motor concentrations, beads detached before reaching the edge of the trap. At the higher concentrations of motors, while moving through and out of the trap, the bead velocity was dependent on load. Both of these findings may be a consequence of a low degree of processivity for ncd, which is consistent with earlier findings from conventional video-based motility assays (our unpublished results). If reconfirmed, this will have important implications for modeling the function of ncd motility and its directionality.

The lateral excursions of a ncd-driven beads were quite large, at least $\pm$100 nm. The maximal lateral excursions allowed by the geometrical constraint of the substrate surface are approximately $\pm$120 nm for a 0.5-μm bead, assuming a zero-length linkage and total freedom of motion of the attachment point of the bead on the microtubule surface (Fig. 13). The data are therefore in sharp contrast to the apparently strong lateral constraints found in tracking of even single kinesin molecules (Gelles et al., 1988; Ray et al., 1993; Wang et al., 1995). However, the bead behavior in our experiments could be a consequence of a flexible and extended connection between bead and microtubule, whereas the motors are faithfully tracking protofilaments.

Spectral analysis of the high-resolution quadrant detector data can shed some light on this problem. The power

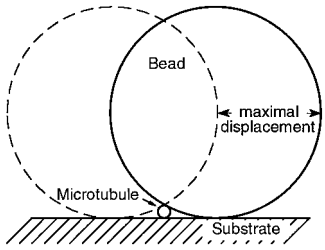

FIGURE 13 Sketch, approximately to scale, of a 0.5-μm bead bound to a microtubule attached to a surface. The maximal possible lateral displacement is $\sim\pm$120 nm.

spectrum contains information about the viscous drag experienced by the bead at high frequencies and, independently of that, information about the elastic constraints in the low-frequency region of the spectrum. Increased drag lowers the corner frequency and decreases the high-frequency amplitudes of the spectrum by the same factor (Eqs. 1 and 2). An increase in horizontal viscous drag is expected in the close vicinity of the surface. If lateral motion is coupled to some degree of vertical displacement (see Fig. 13), the drag coefficient can become very much higher still (Happel and Brenner, 1983).

For both ncd-driven and AMP-PNP-bound stationary beads, the high-frequency regions of the spectra were strongly reduced in amplitude compared with that of an unbound bead (see Fig. 11). This is consistent with a strongly increased drag force very near the surface. The increase in drag by a factor of $\sim$3.5 and 10, respectively, should lower the corner frequency by the same factor. This was not the case for the stationary beads; they thus display an increased stiffness due to attachment through motors and possibly nonspecific binding.

The moving beads, on the other hand, show a decrease in corner frequency by a factor of $\sim$6, which is roughly consistent with the drag increase alone. The fit of the spectrum (Fig. 11) and the simulated data track (Fig. 10 *B*) demonstrate that the lateral motion of the ncd-driven bead looked like simple Brownian motion in a harmonic potential with a drag coefficient close to that of the immobilized beads. The simulated track also demonstrates that it is easy to wrongly identify apparent dwell times that suggest stepping from protofilament to protofilament. The fact that no apparent increase in constraint stiffness is observed (relative to the trap stiffness experienced by the unbound bead) could be due to long and flexible tethers between bead and motors. Such tethers could be formed by aggregates of motors; however, multiple attachments through several motors would tend to limit the lateral excursions strongly if they all stayed processively bound to their protofilaments. Alternatively, if ncd were a low-processivity motor, the bead could perform a fast random walk over the surface. The characteristic sideways stepping time would be related to the cycle time of the motor. This stepping time would have to be fast enough at the saturating ATP concentrations used here to make the motion resemble unhindered thermal motion (constrained to the microtubule surface).

Key experiments for the future, using our or a similar detection method will be to use specific attachments with well characterized compliances (which can be measured by spectral analysis), variation of ATP concentrations to vary the time scale of the motor-driven diffusion process, and variations in trapping stiffness or feedback-controlled beam steering to keep the load exactly zero.

We acknowledge generous technical support from the Rowland Institute for Science, particularly Winfield Hill. We thank Winfried Denk, Ernst Keller, Karel Svoboda, and Steven Block for helpful discussions.

This work has been supported in part by the Whitaker Foundation, the National Science Foundation (grant BIR 95–12699), and by the donors of the Petroleum Research Fund, administered by the American Chemical Society.

REFERENCES

Allen, R. D., G. B. David, and G. Nomarski. 1969. The Zeiss-Nomarski differential interference equipment for transmitted light microscopy. *Z. Wiss. Mikroskopie.* 69:193–221.

Ashkin, A. 1992. Forces of a single-beam gradient laser trap on a dielectric sphere in the ray optics regime. *Biophys. J.* 61:569–582.

Ashkin, A., J. M. Dziedzic, J. E. Bjorkholm, and S. Chu. 1986. Observation of a single-beam gradient force optical trap for dielectric particles. *Opt. Lett.* 11:288–290.

Axelrod, D. 1989. Fluorescence polarization microscopy. *Methods Cell Biol.* 30:333–352.

Barton, J. P., and D. R. Alexander. 1989. Fifth-order corrected electromagnetic field components for a fundamental Gaussian beam. *J. Appl. Phys.* 66:2800–2802.

Barton, J. P., D. R. Alexander, and S. A. Schaub. 1989. Theoretical determination of net radiation force and torque for a spherical particle illuminated by a focused laser beam. *J. Appl. Phys.* 66:4594–4602.

Berliner, E., E. C. Young, K. Anderson, H. K. Mahtani, and J. Gelles. 1995. Failure of a single-headed kinesin to track parallel to microtubule protofilaments. *Nature.* 373:718–721.

Block, S. M., L. S. Goldstein, and B. J. Schnapp. 1990. Bead movement by single kinesin molecules studied with optical tweezers. *Nature.* 348: 348–352.

Born, M., and E. Wolf. 1989. Principles of Optics. Pergamon Press, Oxford.

Brady, S. T. 1985. A novel brain ATPase with properties expected for the fast axonal transport motor. *Nature.* 317:73–75.

Case, R. B., D. W. Pierce, N. HomBooher, C. L. Hart, and R. D. Vale. 1997. The directional preference of kinesin motors is specified by an element outside of the motor catalytic domain. *Cell.* 90:959–966.

Chandra, R., E. D. Salmon, H. P. Erickson, A. Lockhart, and S. A. Endow. 1993. Structural and functional domains of the Drosophila ncd microtubule motor protein. *J. Biol. Chem.* 268:9005–9013.

Coppin, C. M., J. T. Finer, J. A. Spudich, and R. D. Vale. 1996. Detection of sub-8-nm movements of kinesin by high-resolution optical-trap microscopy. *Proc. Natl. Acad. Sci. USA.* 93:1913–1917.

Dekkers, N. H., and H. de Lang. 1974. Differential phase contrast in a STEM. *Optik.* 41:452–456.

Dekkers, N. H., and H. de Lang. 1977. A detection method for producing phase and amplitude images simultaneously in a scanning transmission electron microscope. *Philips Tech. Rev.* 37:1–9.

Denk, W., and W. W. Webb. 1990. Optical measurement of picometer displacements of transparent microscopic objects. *Appl. Opt.* 29: 2382–2391.

Endow, S. A., S. Henikoff, and L. Soler-Niedziela. 1990. Mediation of meiotic and early mitotic chromosome segregation in *Drosophila* by a protein related to kinesin. *Nature.* 345:81–83.

Endow, S. A., S. J. Kang, L. L. Satterwhite, M. D. Rose, V. P. Skeen, and E. D. Salmon. 1994. Yeast Kar3 is a minus-end microtubule motor protein that destabilizes microtubules preferentially at the minus ends. *EMBO J.* 13:2708–2713.

Finer, J. T., R. M. Simmons, and J. A. Spudich. 1994. Single myosin molecule mechanics: piconewton forces and nanometre steps. *Nature.* 368:113–119.

Fritz, M., M. Radmacher, J. P. Cleveland, P. K. Hansma, M. W. Allersma, R. J. Stewart, and C. F. Schmidt. 1995. Imaging microtubules under physiological conditions with atomic force microscopy. *Biophys. J.* 68:A288.

Gauthier, R. C., and S. Wallace. 1995. Optical levitation of spheres: analytical development and numerical computations of the force equations. *J. Opt. Soc. Am. B.* 12:1680–1686.

Gelles, J., B. J. Schnapp, and M. P. Sheetz. 1988. Tracking kinesin-driven movements with nanometre-scale precision. *Nature.* 331:450–453.

Ghislain, L. P., N. A. Switz, and W. W. Webb. 1994. Measurement of small forces using an optical trap. *Rev. Sci. Instrum.* 65:2762–2768.

Ghislain, L. P., and W. W. Webb. 1993. Scanning-force microscope based on an optical trap. *Opt. Lett.* 18:1678–1680.

Gittes, F., E. Meyhöfer, B. Sung, and J. Howard. 1996. Directional loading of the kinesin motor molecule as it buckles a microtubule. *Biophys. J.* 70:418–429.

Gittes, F., and C. F. Schmidt. 1997. Signals and noise in micromechanical measurements. *Methods Cell Biol.* 55:129–156.

Gittes, F., and C. F. Schmidt. 1998. Interference model for back focal plane displacement detection in optical tweezers. *Opt. Lett.* In press.

Gittes, F., B. Schnurr, P. D. Olmsted, F. C. MacKintosh, and C. F. Schmidt. 1997. Microscopic viscoelasticity: shear moduli of soft materials determined from thermal fluctuations. *Phys. Rev. Lett.* 79:3286–3289.

Gouesbet, G., and J. A. Lock. 1994. Rigorous justification of the localized approximation to the beam-shape coefficients in generalized Lorenz-Mie theory. II. Off-axis beams. *J. Opt. Soc. Am. A.* 11:2516–2525.

Hale, G. M., and M. R. Querry. 1973. Optical constants of water in the 200-nm to 200-μm wavelength region. *Appl. Opt.* 12:555–563.

Happel, J., and H. Brenner. 1983. Low Reynolds Number Hydrodynamics: With Special Applications to Particulate Media. Kluwer Academic, Dordrecht, The Netherlands.

Harada, Y., and T. Asakura. 1996. Radiation forces on a dielectric sphere in the Rayleigh scattering regime. *Opt. Commun.* 124:529–541.

Henningsen, U., and M. Schliwa. 1997. Reversal in the direction of movement of a molecular motor. *Nature.* 389:93–96.

Higuchi, H., E. Muto, Y. Inoue, and T. Yanagida. 1997. Kinetics of force generation by single kinesin molecules activated by laser photolysis of caged ATP. *Proc. Natl. Acad. Sci. USA.* 94:4395–4400.

Howard, J., A. J. Hudspeth, and R. D. Vale. 1989. Movement of microtubules by single kinesin molecules. *Nature.* 342:154–158.

Hulst, H. C. 1957. Light Scattering by Small Particles. Wiley, New York.

Ishijima, A., H. Kojima, H. Higuchi, Y. Harada, T. Funatsu, and T. Yanagida. 1996. Multiple- and single-molecule analysis of the actomyosin motor by nanometer-piconewton manipulation with a microneedle: unitary steps and forces. *Biophys. J.* 70:383–400.

Jackson, J. D. 1975. Classical Electrodynamics. Wiley, New York.

Kull, F. J., E. P. Sablin, R. Lau, R. J. Fletterick, and R. D. Vale. 1996. Crystal structure of the kinesin motor domain reveals a structural similarity to myosin. *Nature.* 380:550–555.

Kuriyama, R., M. Kofron, R. Essner, T. Kato, S. Dragas-Granoic, C. K. Omoto, and A. Khodjakov. 1995. Characterization of a minus end-directed kinesin-like motor protein from cultured mammalian cells. *J. Cell Biol.* 129:1049–1059.

Lide, D. R. 1992. CRC Handbook of Chemistry and Physics. CRC Press, Boca Raton, FL.

Lock, J. A., and G. Gouesbet. 1994. Rigorous justification of the localized approximation to the beam-shape coefficients in generalized Lorenz-Mie theory. I. On-axis beams. *J. Opt. Soc. Am. A.* 11:2503–2515.

McDonald, H. B., and L. S. Goldstein. 1990. Identification and characterization of a gene encoding a kinesin-like protein in *Drosophila*. *Cell.* 61:991–1000.

Meyhöfer, E., and J. Howard. 1995. The force generated by a single kinesin molecule against an elastic load. *Proc. Natl. Acad. Sci. USA.* 92: 574–578.

Moore, J. D., and S. A. Endow. 1996. Kinesin proteins: a phylum of motors for microtubule-based motility. *Bioessays.* 18:207–219.

Nomarski, G. 1955. Microinterférомètre différentiel à ondes polarisées. *J. Phys. Radium.* 16:S9–S13.

Press, W. H., B. P. Flannery, S. A. Teukolsky, and W. T. Vetterling. 1992. Numerical Recipes in C: The Art of Scientific Computing. Cambridge University Press, Cambridge, UK.

Ray, S., E. Meyhöfer, R. A. Milligan, and J. Howard. 1993. Kinesin follows the microtubule's protofilament axis. *J. Cell Biol.* 121: 1083–1093.

Sablin, E. P., F. J. Kull, R. Cooke, R. D. Vale, and R. J. Fletterick. 1996. Crystal structure of the motor domain of the kinesin-related motor ncd. *Nature.* 380:555–559.

Schnurr, B., F. Gittes, F. C. MacKintosh, and C. F. Schmidt. 1997. Determining microscopic viscoelasticity in flexible and semiflexible polymer networks from thermal fluctuations. *Macromolecules*. 30: 7781–7792.

Siegman, A. E. 1986. Lasers. University Science Books, Mill Valley, CA.

Simmons, R. M., J. T. Finer, S. Chu, and J. A. Spudich. 1996. Quantitative measurements of force and displacement using an optical trap. *Biophys. J.* 70:1813–1822.

Smith, F. H. 1955. Microscopic interferometry. *Research (London).* 8:385–395.

Smith, S. B., Y. J. Cui, and C. Bustamante. 1996. Overstretching B-DNA: the elastic response of individual double-stranded and single-stranded DNA molecules. *Science.* 271:795–799.

Stewart, R. J., J. P. Thaler, and L. S. Goldstein. 1993. Direction of microtubule movement is an intrinsic property of the motor domains of kinesin heavy chain and *Drosophila* ncd protein. *Proc. Natl. Acad. Sci. USA.* 90:5209–5213.

Svoboda, K., and S. M. Block. 1994a. Biological applications of optical forces. *Annu. Rev. Biophys. Biomol. Struct.* 23:247–285.

Svoboda, K., and S. M. Block. 1994b. Force and velocity measured for single kinesin molecules. *Cell.* 77:773–784.

Svoboda, K., C. F. Schmidt, B. J. Schnapp, and S. M. Block. 1993. Direct observation of kinesin stepping by optical trapping interferometry. *Nature.* 365:721–727.

Vale, R. D., T. Funatsu, D. W. Pierce, L. Romberg, Y. Harada, and T. Yanagida. 1996. Direct observation of single kinesin molecules moving along microtubules. *Nature.* 380:451–453.

Vale, R. D., T. S. Reese, and M. P. Sheetz. 1985. Identification of a novel force-generating protein, kinesin, involved in microtubule-based motility. *Cell.* 42:39–50.

VanBuren, P., S. S. Work, and D. M. Warshaw. 1994. Enhanced force generation by smooth muscle myosin in vitro. *Proc. Natl. Acad. Sci. USA.* 91:202–205.

Visscher, K., S. P. Gross, and S. M. Block. 1996. Construction of multiple-beam optical traps with nanometer-resolution position sensing. *IEEE J. Quantum Electron.* 2:1066–1076.

Walker, R. A., E. D. Salmon, and S. A. Endow. 1990. The *Drosophila* claret segregation protein is a minus-end directed motor molecule. *Nature.* 347:780–782.

Wang, Z., S. Khan, and M. P. Sheetz. 1995. Single cytoplasmic dynein molecule movements: characterization and comparison with kinesin. *Biophys. J.* 69:2011–2023.

Wang, M. D., H. Yin, R. Landick, J. Gelles, and S. M. Block. 1997. Stretching DNA with optical tweezers. *Biophys. J.* 72:1335–1346.

Williams, R. C., Jr., and J. C. Lee. 1982. Preparation of tubulin from brain. *Methods Enzymol.* 85(Pt B):376–385.

Wilson, T. 1988. Enhanced differential phase contrast imaging in scanning microscopy using a quadrant detector. *Optik.* 80:167–170.

Yin, H., M. D. Wang, K. Svoboda, R. Landick, S. M. Block, and J. Gelles. 1995. Transcription against an applied force. *Science.* 270:1653–1657.

Yoshida, A., and T. Asakura. 1974. Electromagnetic field near the focus of Gaussian beams. *Optik.* 41:281–292.